The impact of the melting layer on the passive microwave cloud scattering signal observed from satellites: A study using TRMM microwave passive and active measurements

V. S. Galligani,[1] C. Prigent,[1] E. Defer,[1] C. Jimenez,[1] and P. Eriksson[2]

[1] Concurrent passive and active microwave measurements onboard the Tropical Rainfall Measurement Mission (TRMM) show that under cloudy conditions, when a melting layer is detected by the precipitation radar, a polarized scattering signal at 85 GHz in passive mode is often observed. Radiative transfer simulations confirm the role of large horizontally oriented non-spherical particles on the polarized scattering signal and assess the effect of changes in particle phase, from solid ice to dry snow to melting snow, on the radiative properties. We conclude on the necessity to account for this polarization generated by the clouds in passive microwave rain retrievals and to use this specific signature to help diagnose the precipitation type and derive more accurate algorithms. In addition, analysis of the passive microwave polarized scattering is a unique way to get insight into microphysical properties of clouds at global scale, and this potential should be explored at millimeter and submillimeter frequencies that are more sensitive to the scattering generated by smaller particles.

1. Introduction

[2] Several methods for estimating instantaneous precipitation rates from combined passive and active space-borne microwave observations have been developed and applied. These retrieval methods depend on the accuracy of the relationships between precipitating cloud properties and microwave observables. The lack of direct knowledge of the microphysical and associated radiative properties of certain precipitation particles like melting hydrometeors, which have an important radiative impact in stratiform regions, have led to subjective assumptions in the retrieval algorithms. In the stratiform regions of clouds, particles undergo complex melting processes as they fall through the freezing level. These processes have been described through aircraft microphysical measurements [e.g., *Willis and Heymsfield*, 1989], tunnel experiments [e.g., *Mitra et al.*, 1990] and modeling studies [e.g., *Zawadzki et al.*, 2005]. Around the 0°C isotherm, the aggregation of snow particles of different sizes and fall velocities forms larger flakes of similar velocity, leading to a large increase in the maximum-sized particles and a decrease in the total number of concentration. The low density flakes start to melt and turn into a mixture of water, ice, and air. During the melting process, the flakes collapse into raindrops of much smaller size than the original flakes of the same mass, but with an increased fall speed, yielding smaller particle concentration. Snow flakes typically melt within 100 to 500 m, and ice particles can be present at temperatures as high as 5°C.

[3] An increase in the radar backscattered signal close to the freezing level in stratified clouds, the so-called bright band, has been observed by ground based weather radars as early as the 1940s, and it was interpreted in terms of the melting of snow flakes [*Cunningham*, 1947]. Since the real part of the dielectric constant of water is more than three times larger than that of ice at 37 GHz, for example, the scattering caused by raindrops is greater than the one caused by ice particles of the same size. In the melting layer, wet snow flakes behave like large water drops, enhancing the backscattering whereas in the melted layer below, the decrease in number concentration and in particle size acts to reduce the radar reflectivity. The contrast between the higher reflectivity in the melting layer and the lower reflectivity below produces a bright band in the radar response, especially at low frequencies where attenuation by rain is not significant as seen from space. The signature of the melting layer is also significant from satellite instruments as observed with the Precipitation Radar (PR) onboard the Tropical Rainfall Measurement Mission (TRMM) since 1997. When the

[1]Laboratoire d'Etudes du Rayonnement et de la Matière en Astro-physique (LERMA), Centre National de la Recherche Scientifique, Observatoire de Paris, Paris, France.

[2]Department of Earth and Space Sciences, Chalmers University of Technology, Gothenburg, Sweden.

Corresponding author: V. S. Galligani, Laboratoire d'Etudes du Rayonnement et de la Matière en Astro-physique (LERMA), Centre National de la Recherche Scientifique, Observatoire de Paris, Paris, France. (victoria.galligani@obspm.fr)

bright band is detected with the PR at 13 GHz, its effect on the reflectivity profile is taken into account in the rain retrieval algorithms. At CloudSat higher frequency, 94 GHz, only a sharp increase in the backscattering is observed at the melting layer: the decrease in the backscattering measured by TRMM at 13 GHz is not observed at 94 GHz due to the significant attenuation by rain [*Di Girolamo et al.*, 2003; *Kollias and Albrecht*, 2005; *Sassen et al.*, 2007].

[4] The impact of the melting layer on passive microwave observations has also been explored, mainly through modeling studies [*Bauer et al.*, 1999, 2000; *Olson et al.*, 2001a, 2001b]. Rather detailed melting processes have been implemented in cloud resolving models to produce realistic hydrometeor profiles, later used in radiative transfer simulations along with various dielectric models, size, and density distributions. The advanced melting scheme developed by *Olson et al.* [2001b] includes melting evaporation, particle interaction, and the effect of changing particle density within a three-dimensional cloud model over the radiatively cold ocean. Other simulation studies have also focused on the modeling of the dielectric properties of the mixed-phase melting particles [e.g., *Meneghini and Liao*, 1996, 2000]. All these studies result in an increase of the brightness temperatures (TBs) when the bright band is present. *Olson et al.* [2001a] found an increase of the TBs up to 15, 12, and 9 K at 19, 37, and 85 GHz respectively. From observations around a North Atlantic cyclone with SSM/I along with aircraft microphysical measurements, *Schols et al.* [1999] concluded that melting snow aggregates generate rather high TBs at 85 GHz compared to the regions where dense ice particles are present. *Battaglia et al.* [2003] conducted the first systematic analysis of observations to explore the effect of the melting layer on the passive microwave signal by looking at coincident radar and passive microwave observations during 5 years of TRMM data from December, January, and February over the East Pacific. They focus on frequencies below 40 GHz and conclude that the bright band has a significant impact on the microwave signal. At 10 and 19 GHz, at constant rain rate, the average TBs are always higher in the presence of a bright band suggesting the significant role of emission at those frequencies. The average TB difference read between presence and absence of the bright band decreases with increasing rain rate at 19 and 37 GHz, but at 85 GHz, TBs are lower in presence of a bright band, contradicting previous results (essentially from simulations) and suggesting the importance of the scattering effect above the melting layer. This scattering signal at 85 GHz has been used, for example, by *Mohr et al.* [1999] to estimate precipitation over ocean and land.

[5] In this study, we explore the impact of particle phase changes around the melting layer on the passive microwave observations using combined passive and active observations from TRMM, and we focus on the TRMM Microwave Imager (TMI) radiometric signatures. The PR and the TMI instruments provide simultaneous passive and active microwave observations, respectively, that document the hydrometeor contents of the sampled clouds at different wavelengths [*Kummerow et al.*, 1998, 2000]. We already analyzed the scattering polarized signatures at 85 GHz, with the help of coincident infrared observations from the International Satellite Cloud and Climatology Project (ISCCP) data set [*Prigent et al.*, 2001] and with the Lightning

Imaging Sensor (LIS) [*Prigent et al.*, 2005]. We established the relationship between negative polarized signatures (difference between vertically and horizontally polarized brightness temperatures) at 85 GHz and the lightning activity in convective cores. Radiative transfer simulations showed that negative polarization differences can be explained by relatively large non-spherical particles, mostly vertically oriented. This is in contrast to small horizontally aligned plates populating cirrus clouds and large frozen particles in the form of aggregates that exhibit a horizontal preferential alignment due to aero-dynamical effects [*Xie and Miao*, 2011; *Xie et al.*, 2012]. In this study, we analyze TMI 37 and 85 GHz radiometric signals sensed in clouds and more specifically in bright band cloud regions based on PR measurements. The methodology and the data are described in section 2. Section 3 presents the observational results that suggest that polarized scattering at 85 GHz coincides with the presence of a melting layer. Section 4 uses radiative transfer simulations to examine the link between polarized scattering in the microwave and the properties of the hydrometeors, essentially their phase and density. Section 5 concludes this study, insisting on the interest of the analysis of the polarized signal at 85 GHz for more accurate precipitation retrievals.

2. The TRMM Observations

[6] The TRMM satellite, launched in 1997, carries a suite of instruments designed to study precipitation in the tropics [*Kummerow et al.*, 1998]. It includes two microwave instruments, one passive and one active, which are both used in this study. The TMI, a conical imager, measures at 10.7, 19.4, 21.3, 37, and 85.5 GHz with two orthogonal polarizations (except at 22 GHz) and a spatial resolution between 63 km × 37 km and 7 km × 5 km, depending on the frequency, and a swath of 780 km. The PR observes at 13.8 GHz with a 4 km resolution and a swath of 220 km located in the center of the TMI swath.

[7] The precipitation properties (near surface rain rate, convective/stratiform rain, and bright band properties) emanate from the 2A23 and 2A25 PR products. The algorithm 2A25 uses a Z-R relationship based on a particle size distribution model and retrieves profiles of the radar reflectivity factor with rain attenuation correction and rain rate for each radar beam [*Iguchi et al.*, 2000]. The algorithm 2A23 verifies if a bright band exists in rain echoes and determines the bright band height and intensity when it exists [*Awaka et al.*, 1997]. The rain type is classified into stratiform, convective and others, based on the detection of BB and, in case of warm rain, on the horizontal structure of the reflectivity field. The PR minimum detectable rain is usually considered to be 0.5 mm h^{-1}. *Schumacher and Houze* [2000] derive maps of rainfall rate and convective/stratiform classification for oceanic cases that compare well between PR and S-band validation radar records during the Kwajex experiment. *Schumacher and Houze* [2000] also report a tendency of the PR to under sample weaker echoes associated with stratiform rain near the surface and ice particles aloft, but the PR is still able to record most of the near-surface precipitation accumulation. *Liao and Meneghini* [2009] showed a fairly good agreement between the PR and Melbourne Weather Surveillance Radar-1988 Doppler
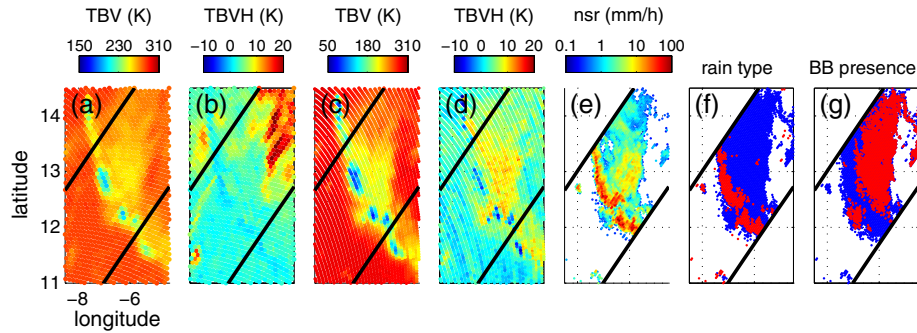
Figure 1. TRMM observations of a squall line in Africa during the AMMA campaign (19 August 2006) with (a) TBV(37 GHz), (b) TBVH(37 GHz), (c) TBV(85 GHz), (d) TBVH(85 GHz), (e) the near surface rain rate, (f) the PR rain type flag from the 2A23 PR product, convective in red and stratiform in blue, and (g) the presence of a BB in red.

(WSR) derived rain rates for the case of stratiform rain, while during convective rain the PR seems to overestimate light rain, and underestimate moderate to heavy rain in comparison with the WSR data, but different performances are expected worldwide, according to variability in climate, surface background, and raindrop size distributions [*Liao and Meneghini*, 2009]. More recently the analysis performed by *Berg et al.* [2010] reported a rather good agreement between PR and Cloud Profiling Radar (CPR) rain rates for the range 1 to 3 mm h^{-1} for a total precipitable water (TPW) estimate above 40 mm. In the present study, the PR observations are considered as valid and accurate enough to describe the properties of the precipitation (e.g., geographical distribution, rain rate type, and rain rate).

[8] TMI and PR observations, together with its derived products, have been merged together on a regular 0.2° × 0.2° grid mesh for 2 years (2006 and 2007). Each grid box contains, when available, the TMI 1B11 brightness temperatures located within the box, the TMI 2A12 derived rain parameters (not used in the analysis), and the PR level 2A products 2A23 and 2A25. The analysis of the database is performed over sea and land separately based on the 2A12 surface flag. In order to avoid contamination of the radiometric signal by snow on the ground, snow-covered pixels are filtered out using the National Snow and Ice Data Center (NSIDC) data [*Armstrong and Brodzik*, 2005].

3. Analysis of the Polarized Scattering Signatures of TMI Data in the Presence of Melting Layer

[9] A case study at a pixel level is presented in Figure 1 over land. It corresponds to a squall line in Africa as observed during the African Monsoon Multidisciplinary Analyses (AMMA) campaign (19 July 1998). Averaged vertical and horizontal brightness temperatures (TBV and TBH) and their polarization differences (TBVH) are shown in Figure 1. TBVH(85 GHz) signals of the order of 8 K and TBV(85 GHz) signals of the order of 220 K when the PR detects stratiform rain and the presence of BB can be observed, as presented by the statistical analysis that follows. Similarly, at 37 GHz some scattering is observed with the convective phase with lower TBVs but little polarization difference. In the stratiform part of the cloud, less pronounced scattering is present compared to 85 GHz. Near surface rain

rate as provided by PR ranges over two orders of magnitude in the stratiform region in presence or not of BB. Regions of convective rain where there is no BB reported shows very low TBVs and negative or negligible polarization signals, high rain rate, and lightning activity (not shown).

[10] In order to assess the impact of the melting layer on the TMI observations, cases of stratiform rain are first identified with the PR and further divided into cases with and without melting layers as detected by the PR bright band (BB). Stratiform rain boxes of 0.2° × 0.2° are identified as having at least 20 PR observations with 50% of them stratiform; considered in this study are only those boxes where the bright band is detected for 100% of stratiform observations or for 0% of them. TBV, TBH, and TBVH at TMI frequencies are analyzed as a function of the stratiform near surface rain rate, with and without a melting layer. Figure 2 presents the variations as a function of stratiform rain rate of the TBH and TBVH over ocean (Figures 2a–2j) and land (Figures 2k–2t), along with their standard deviations, computed over the 0.2° × 0.2° grid at 37 and 85 GHz for stratiform rain with a BB (blue curve) and without a BB (red curve).

[11] The ocean has a rather low surface emissivity, with large polarization differences. At low frequencies, emission by cloud and rain increases the TBs over the radiometrically cold background, and the polarization generated by the surface decreases with increasing cloud and rain attenuation. For all frequencies above 10 GHz, the presence of BB tends to decrease the TBs. At 85 GHz, two phenomena compete, namely the emission and the scattering by cloud and rain. The difference between the presence and absence of a bright band is evidenced clearly at 85 GHz over land for high rain rates. TBs are lower when a BB is detected, likely associated with the increasing number of frozen particles associated to the melting layer. In addition TBs decrease with increasing RR for BB cases. The difference between BB and no-BB polarization difference increases with increasing rain rate, i.e., increasing ice quantities. This is clear evidence that the polarization difference (of the order of 7K) is generated by the hydrometeors, not by the polarized surface of the ocean.

[12] Land surface emissivities in the microwave region are usually very high (above 0.95) and low polarization differences, and the cloud and rain emission signatures are more difficult to detect due to the lack of contrast between the
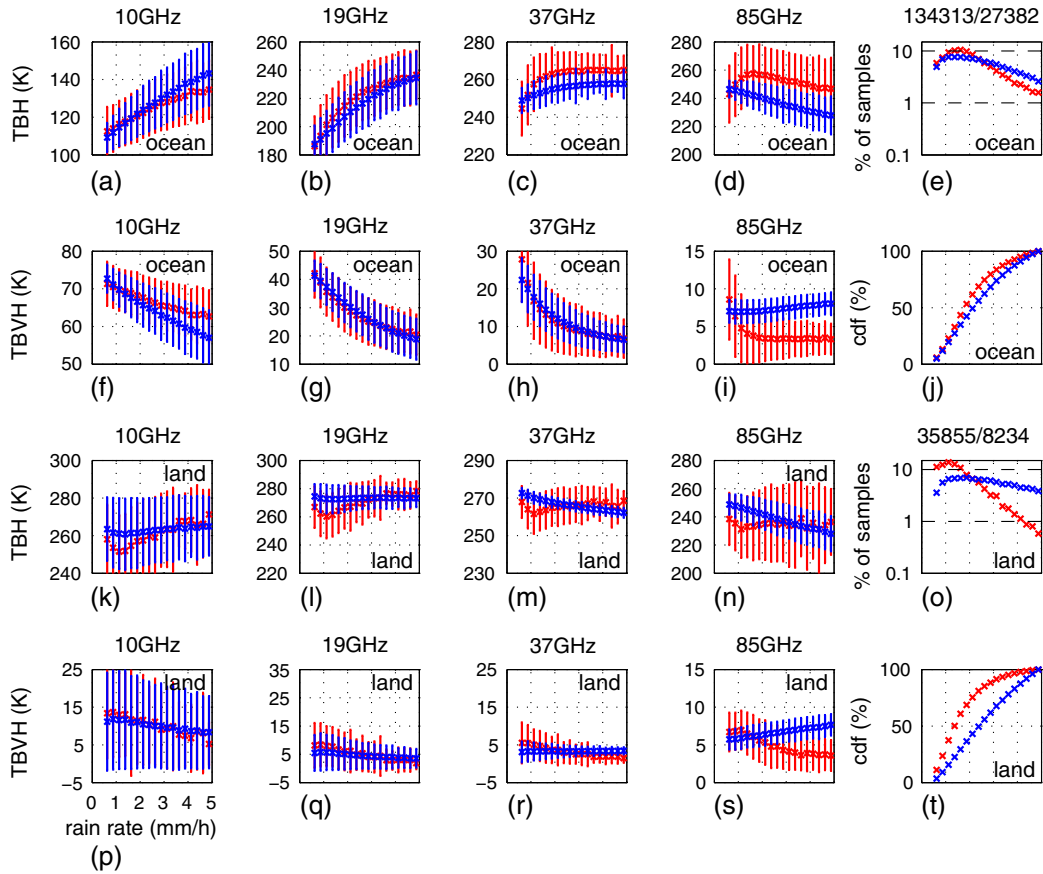
Figure 2. Variations of TMI (a–e, k–o) averaged brightness temperatures (TBH) and (f–j, p–t) averaged polarization differences (TBVH) along with their standard deviations as a function of the averaged rain rate as computed over a $0.2° \times 0.2°$ grid over 2 years for the Tropical region. The $0.2° \times 0.2°$ rain boxes are identified as having at least 20 PR observations with 50% of them being stratiform. Blue (red) represents grid boxes where the bright band (BB) was detected for 100% (0%) of stratiform observations. Figure 2e (Figure 2o) presents the percentages of grid-boxes relative to the total number of grid-boxes (indicated at the top of the panel—with/without BB) that satisfy the selection criteria as a function of rain rate over ocean (land). Their respective cumulative distribution function as a function of rain rate for cases with a BB (blue) and without a BB (red) is shown in Figures 2j and 2t for ocean and land, respectively.

surface and the atmosphere contributions. At 37 and 85 GHz, the variation of the brightness temperatures in presence of BB decreases for an increasing rain rate while the average brightness temperature is more or less constant in stratiform rain without a melting layer. The scattering signal by frozen particles is not only observable at 85 GHz when a melting layer is detected, but also at 37 GHz. Note nevertheless that, as expected, the magnitude of the TB decrease at 37 GHz is much more limited than at 85 GHz. Similar to what is observed over ocean, the polarization difference increases with increasing rain rate. On the average, a polarization difference of 4–5 K is observed for a rain rate of 5 mm/h between cases with and without melting layer.

[13] A sensitivity study (not shown) of the different thresholds over ocean shows that decreasing the percentage of BB for a given rain rate of 85 GHz induces warmer TBs, a decrease of the polarization difference, and a larger standard deviation of both TBs and polarization difference. When one increases the percentage of stratiform pixels, the number of non-BB rain pixels decreases and the averaged brightness temperatures get warmer at 85 GHz.

[14] Figure 3 presents the probability of precipitation cases (precipitation, convective precipitation, stratiform precipitation, and precipitation with BB) at 85 GHz as a function of TBV and TBVH using 2 years of data over both ocean and land, for 1 K × 1 K pairs of TBVH versus TBH. The probability of precipitation is defined as the averaged value of the number of PR pixels identified as precipitation divided by the number of PR observations within the same box. Only cases at least partly precipitating are considered, representing approximately 5% of the total population over both surfaces. In the case of precipitation over ocean (Figure 3a), the vertical branch with large polarization differences corresponds to situations with partial transmission of the surface's polarized signal despite the rain attenuation. The horizontal branch in the scatter plots corresponds to the decreasing TBs associated with the scattering signal of clouds. As expected, the probability of rain increases when the brightness temperatures decrease, i.e., when the convection deepens. Figure 3b (ocean) and Figure 3f (land) further show the percentage of PR pixels identified as convective rain pixels divided by the number
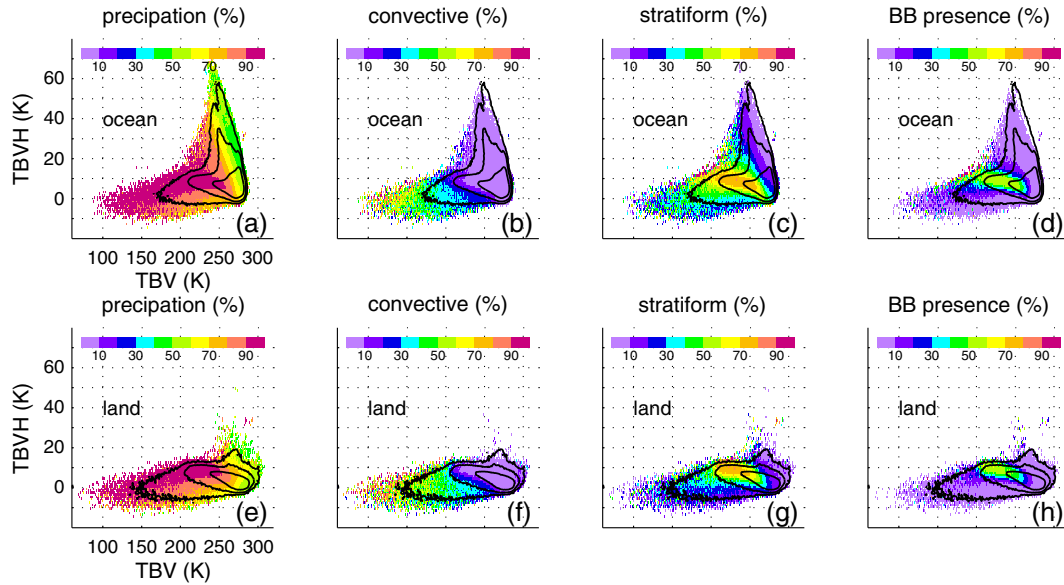
Figure 3. Scatter plot of the polarization difference (TBVH) versus the vertical polarization (TBV) at 85 GHz, for 2006 and 2007 data, over ocean (top) and over land (bottom), of the (a and e) probability of precipitation, of (b and f) convective rain, of (c and g) stratiform rain, and of (d and h) the presence of a BB. Black iso-lines delineate the population that represents 10^{-3}, 10^{-2}, and 0.1% of the total number of samples.

of PR observations within the same box. Colder brightness temperatures are more often observed over land than over ocean, which is consistent with the fact that continental convection is deeper than oceanic convection; deeper convection inducing more ice in the clouds and, consequently, more efficient scattering by large ice particles. Additionally, cold brightness temperatures associated with deep convection can exhibit negative polarization differences. *Prigent et al.* [2005] explain such radiometric behavior by the presence of predominantly vertically oriented graupel located in the convective cores. Convective rain (Figures 3b and 3f) and stratiform rain (Figures 3c and 3g) are clearly reported in two different regions of the TBV/TBVH space over both ocean and land. Convective rain is basically expected where TBVs at 85 GHz are below 250 K with a polarization difference negative or slightly positive. Stratiform rain is statistically dominant for TBV ranging from 200 K to 260 K and a positive TBVH from 5 K. Some basic threshold delimiting the specific regions of the TBVH space could be used as convective/stratiform classification for microwave-based retrieval schemes for TMI, but also for other space missions with similar frequencies and footprints after cross-calibration of the microwave sensors.

[15] For stratiform rain, one can expect a large spatial distribution of the rain field and a relatively homogeneous microwave signal within the box. Brightness temperatures with low percentage of stratiform rain correspond to clouds where there is also convection sampled in the same grid box. Note also that the sum of convective rain probability and stratiform rain probability is not necessarily equal to 100% because some of the PR pixels can be classified as non convective and non stratiform. Finally, Figure 3d (and Figure 3h) presents how the signal at 85 GHz correlates with the presence of BB over ocean (and land). Interestingly the high probability of BB presence spans over a relatively

limited domain in the TBVH space around 7 K and, as expected, the high percentage of BB presence corresponds to regions where stratiform rain is also predominantly detected.

[16] For comparison, Figure 4 presents similar plots to Figure 3 but at 37 GHz. Stratiform and convective rains are clearly reported in two separate regions of the TBVH space for both ocean and land. Convective rain is predominantly detected (>70%) for brightness temperatures below 250 K and polarization differences up to 10 K (Figure 4b). Colder brightness temperatures can be recorded over land, because of more intense and therefore deeper convection over surfaces that can undergo strong solar heating. Stratiform rain (Figure 4c) is recorded for a large range of brightness temperatures (220 to 280 K) and a positive polarization difference of up to 40 K. Over land, the distribution peaks lie in a relative narrow area in the TBVH space.

[17] The possible links between the polarized scattering signatures at 85 GHz and the polarized observations in the visible [*Noel and Chepfer*, 2004; *Bréon and Dubrulle*, 2004] have also been investigated (Appendix A), but the relationship between the two phenomena was not conclusive.

4. Modeling the Sensitivity of the Passive Microwave Signal to Changes in Hydrometeor Phases

[18] As discussed, the melting layer is primarily characterized by a change in the particle composition from ice (more precisely a mixture of ice and air) to liquid water. This transformation has multiple impacts in terms of particle size, number concentration, and possibly shape and orientation. Our objective here is to assess qualitatively how changes in hydrometeor dielectric properties impact the polarized scattering signal in passive observations to investigate on the possible link between polarized scattering on the microwave
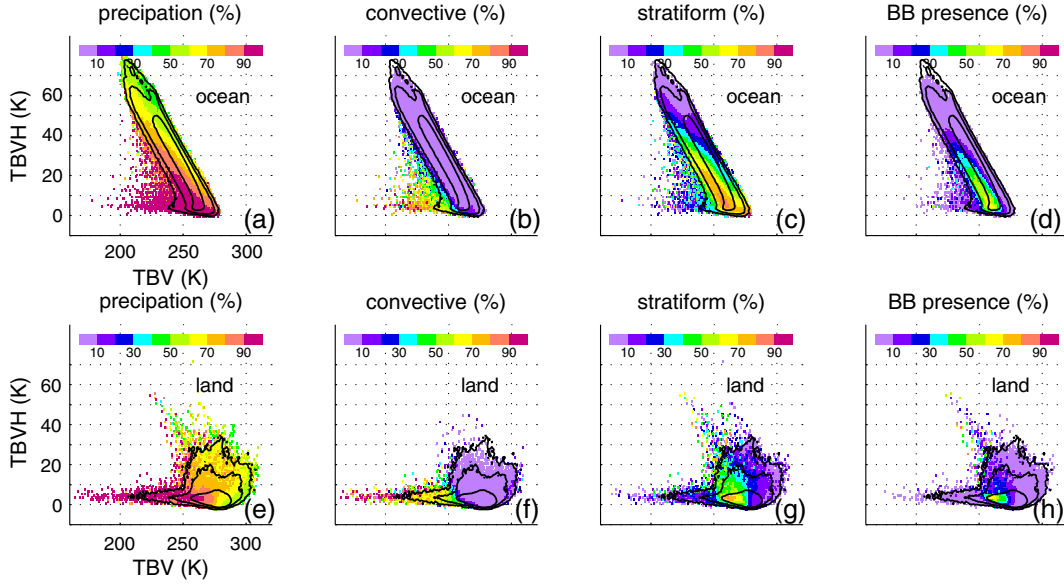
Figure 4. Same as Figure 3 but for 37 GHz.

and the dielectric properties in the BB melting layer. What causes the strongly polarized scattering signal observed at 85 GHz in stratiform situations? How do pure ice and snow compare in terms of scattering at 85 GHz for realistic particle habits? Does the snow wetness enhance the scattering effect and compensate for the decrease in size a melting particle goes through?

4.1. Dielectric Properties

[19] Water, air, and ice coexist in a single particle during the melting process. There is a large number of mixing formulas available to compute the effective dielectric constants of mixed phase hydrometeors and their results vary to a great extent when defining the order of the inclusions, being physically unclear as to how to select among these various formulas. Questions remain as to which of these mixing formulas can be applied to computations of polarimetric parameters from non-spherical melting particles. Furthermore, *Botta et al.* [2010] showed that the scattering behaviors as calculated from effective dielectric properties must be used with caution particularly at millimeter wavelengths. In summary, there are many ways to model the dielectric properties of mixtures which can directly lead to variabilities in the modelled BB effects [*Kollias and Albrecht*, 2005]. A review of the effective dielectric constants of mixed phase hydrometeors is proposed by *Meneghini and Liao* [2000].

[20] *Liao and Meneghini* [2005] insist that the effective dielectric properties of particles in the melting layer are the key problem in the simulation of the bright band signal in the active mode. *Kollias and Albrecht* [2005] assume that the physical model of the melting layer is correct and only test the reflectivity (i.e., the scattering properties) of the corresponding hydrometeor profiles. *Sassen et al.* [2007] argue that the details within the narrow melting layer are not too important because ultimately it is the difference between the scattering properties in the two phases that matters.

[21] *Meneghini and Liao* [2000] reviewed some of the available models and investigated their effect on extinction and backscattering coefficients at radar wavelengths and

concluded that the Maxwell Garnett mixing rule for an air-ice mixture in a water matrix compares best to the Fast Fourier Transform numerical method. Since then, the Maxwell Garnett formulation has been commonly used [e.g., *Battaglia et al.*, 2003; *Olson et al.*, 2001a, 2001b]. Under this formulation, the effective dielectric constant (ϵ_{eff}) is

$$\epsilon_{\text{eff}} = \epsilon_{\text{mat}} + 3f\epsilon_{\text{mat}} \frac{(\epsilon_{\text{inc}} - \epsilon_{\text{mat}})}{\epsilon_{\text{inc}} + 2\epsilon_{\text{mat}} - f(\epsilon_{\text{inc}} - \epsilon_{\text{mat}})} \quad (1)$$

where ϵ_{mat} and ϵ_{inc} are the dielectric constants of the matrix and the inclusion phases respectively, and f is the volume fraction of the inclusions. Under the Maxwell Garnett formulation, snow is often described as a two phase mixture of ice-air (dry snow) and water. Its uniform density (ρ_m) varies with the melted fraction f_m, i.e., the volume fraction of water, as

$$\rho_m = \frac{\rho_s \rho_w}{f_m \rho_s + (1 - f_m)\rho_w} \quad (2)$$

where ρ_s and ρ_w are the density of dry snow and water, respectively. However, questions still remain as to how these three-phase mixtures are composed. A variety of different models arises depending on how the inclusion phases are defined, described well in *Fabry and Szyrmer* [1999] and *Brown and Ruf* [2007].

[22] *Olson et al.* [2001a, 2001b] conducted an intercomparison of dielectric models at 10.65, 19.35, 37.0, and 85.5 GHz for melting snow and graupel, showing that the refractive index curves of these hydrometeors were bounded by the Maxwell Garnett water matrix with ice inclusions (MGwi) and the Maxwell Garnett ice matrix with water inclusions (MGiw) model curves. *Olson et al.* [2001a, 2001b] also noted that the refractive indices of snow and graupel are subtly different, and their differences decrease as the meltwater fraction increases, and that overall, particle absorption and scattering efficiencies in these frequencies are enhanced greatly for relatively small meltwater fractions.

[23] In this study we use a model which literature has shown to agree with the average characteristics of the

Table 1. Density (ρ_s(D)) Parameterizations Used[a]

Label	Parameterization	Details
MA	$\rho_s = 0.015D_s^{-1}$	*Fabry and Szyrmer* [1999] relationship, as in *Mitchell et al.* [1990] and averaged for all types of snow.
MB	$\rho_s = 0.012D_s^{-1}$	*Fabry and Szyrmer* [1999] modification of the above relationship.
LH	$\rho_s = 0.015D_s^{-1.18}$	*Locatelli and Hobbs* [1974] relationship with assumptions made in *Fabry and Szyrmer* [1999].

[a]Equations are given in cgs units.

melting layer for long term observations [*Olson et al.*, 2001a, 2001b; *Battaglia et al.*, 2003; *Fabry and Szyrmer*, 1999; *Zawadzki et al.*, 2005]. This model applies equation (1) twice: one time to calculate dry snow (ice inclusions in an air matrix) and a second time to mix dry snow and water (water inclusions of melted volume fraction f_m in a dry snow environment). An important parameter left to define is the density of the snow, well known to decrease rapidly with size. Different relationships are seen in the literature where the upper limit is the density of pure ice (0.917 gcm^{-3}). Here a number of parameterizations found in the literature (see Table 1) are used to define ρ_s in equation (2). The overall density of the wet snow particle then follows equation (2).

4.2. Radiative Transfer Calculations

[24] Radiative properties of the melting layer are sensitive to a large number of parameters, such as the choice of dielectric models, density parameterization, or the integrated water paths (IWP, defined as the hydrometeor, ice, snow, or melting snow, column integrated water mass). Here we attempt to asses the sensitivity to such parameters in passive microwave observations.

[25] The Atmospheric Radiative Transfer Simulator (ARTS) is adopted for the sensitivity analysis. ARTS is a freely available, open source, software package with state-of-the-art gaseous absorption estimation and able to handle scattering (and full account of polarization effects) very efficiently [*Eriksson et al.*, 2011]. The discrete ordinate iterative (DOIT) method is one of the scattering algorithms in ARTS [*Emde et al.*, 2004] and the one used in this study. Tests were also conducted using the Monte Carlo method available in ARTS and similar results were found. The optical (single scattering) properties were calculated using the T-matrix code by *Mishchenko* [2000] which allows the treatment of oriented spheroids. It is important to keep in mind that modeling the optical properties of frozen particles is problematic even for pristine frozen particles that are not undergoing melting. The particle size distribution, the dielectric properties of the material, and the shape of the particle are all subject to large uncertainties that can translate into significant differences in terms of simulated brightness temperatures [e.g., *Surussavadee and Staelin*, 2006; *Meirold-Mautner et al.*, 2006; *Kulie et al.*, 2010].

[26] For the simulations in this study, a given atmospheric profile of temperature, pressure, water vapor, ozone, and height from the *Chevallier et al.* [2006] database was used
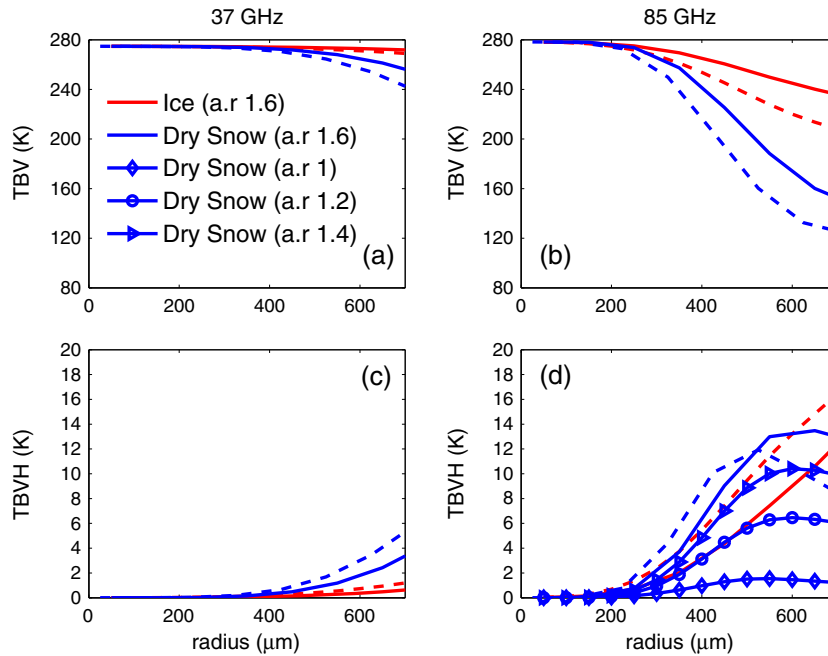

Figure 5. (a and b) The sensitivity of the vertical brightness temperature (TBV) and (c and d) the polarization difference (TBVH) at 37 and 85 GHz to the particle size (effective radius) of horizontally aligned pure ice and dry snow spheroids of aspect ratio 1.6, under different IWPs (solid lines for 0.2 kg/m^2 and dashed lines for 0.4 kg/m^2). Dry snow is composed of ice inclusions in an air matrix such that its density is parameterized by MA in Table 1. Additionally, the simulated polarization difference at 85 GHz for dry snow (0.2 kg/m^2) of different aspect ratios were added in Figure 5d.
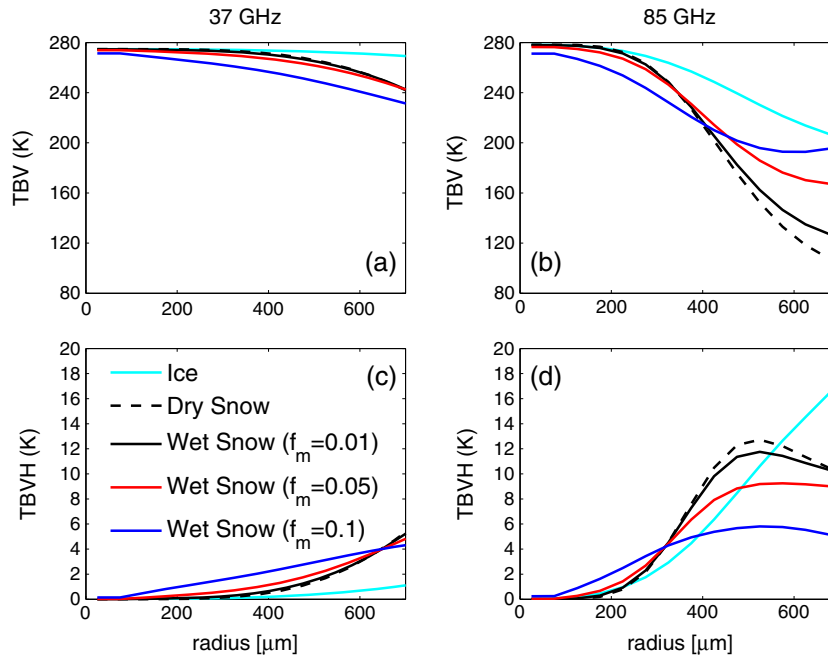
Figure 6. The simulated vertical polarization and polarization difference at 37 and 85 GHz for pure ice and wet snow hydrometeors (air-ice-water mixture) using the Maxwell Garnett mixing rule for a two phase mixture (air and ice) and water. Different melted fractions (f_m) are shown. The IWP is 0.4 kg/m^2.

(atmosphere of 8.3 kg/m^2 of water vapor). The land surface emissivity in the simulations is set to 0.9 for both polarizations and the nadir angle is set to 50°. A single layer (2 km thick) of hydrometeors populates the atmosphere around the 0° isotherm (4 km in altitude) with varying IWP (between 0.1 kg/m^2 and 2 kg/m^2). A mono-disperse particle size distribution of horizontally orientated spheroids was assumed and varied between 50 μm-700 μm (size refers to the size of a mass equivalent sphere).

[27] Simulations with hydrometeor profiles of more realistic characteristics (three plane parallel hydrometeor layers) are also analyzed (now shown). The three layers were composed of the following: (1) a layer of ice particles between 5 and 8 km with an equivalent ice water path of 0.4 kg/m^2 and single-size spherical randomly orientated particles of 150 μm radius; (2) a layer representing the melting layer between 3 and 5 km as described above; and (3) a rain layer of 4 mm/hr between 0 and 3 km containing liquid water, single size spherical randomly orientated particles of 400 μm radius. Such hydrometeor profiles yield similar results in terms of polarization difference at 85 GHz than the melting layer alone. The ice cloud above only adds limited extinction to the signal (a decrease of the polarization difference smaller than 2 K), and the rain below is not observed as the melting layer is quite opaque. We focus thus on the parameters of the particles populating the melting layer relevant to the observed polarized scattering signals described earlier in the presence of a BB, by simplifying the hydrometeor profiles to just the melting layer.

[28] With respect to defining the shape of these hydrometeors for the purpose of modeling the radar bright band at TRMM frequencies, the precise particle shapes are not very important, and scattering properties depend mostly on the overall shape of the particles as determined by the aspect ratio [*Dungey and Bohren*, 1993; *Matrosov et al.*, 2005].

From multiple aircraft observations, Heymsfield (personal communication, 2005) confirms the importance of the bulk aspect of particles as characterized by its aspect ratio, neglecting the simulation of individual complicated particle shapes: aspect ratios (longest/shortest axis of ellipse) of the order of 1.6 close to the 0° isotherm are selected, as suggested in *Korolev and Isaac* [2003]; *Hanesch* [1999]; and *Matrosov et al.* [2005].

[29] Considered in this study are perfectly horizontally aligned particles. Most particles are likely to suffer particle tumbling related to turbulence. The effect of tumbling has already been evaluated in *Prigent et al.* [2001]. *Xie et al.* [2012] showed that horizontally aligned particles behave similarly to oriented particles with a standard deviation of 10°, with TBs and polarization differences deviating less than 0.2 K compared to the perfect horizontal case. In this study, we will concentrate on perfectly horizontally aligned particles, for practical reasons.

[30] *Prigent et al.* [2005, 2001] explained the observed polarized scattering signal of pristine ice habits in terms of particle shape and orientation, where simulations with randomly oriented, large spheroidal particles cannot replicate the observed polarization differences at 85 GHz, but oriented non-spherical particles can. Following these studies, Figures 5a and 5b (resp. Figures 5c and 5d) show the vertical brightness temperature, TBV, (resp. polarization differences, TBVH) for 37 and 85 GHz as a function of particle size for pristine, horizontally distributed ice (ρ=0.917 kg/m^3) of aspect ratio 1.6. As expected, the TBVs decrease with increasing particle size, especially at 85 GHz: the larger the IWP, the larger the depression. In terms of the polarization signal, differences at 85 GHz also increase with increasing particle size and with increasing IWP. To evaluate the sensitivity of the scattering signal to particle composition, Figure 5 also shows the TBV and TBVH for dry snow
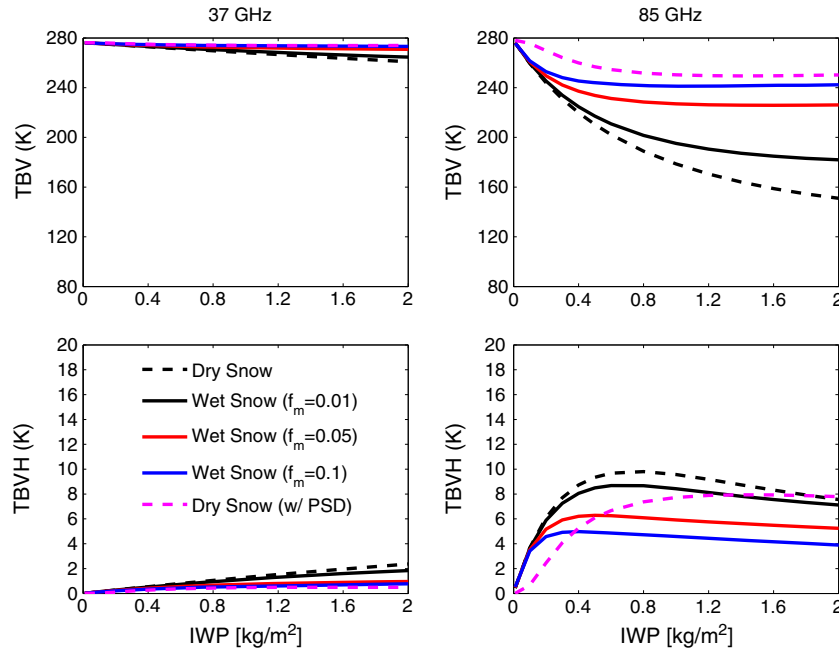
Figure 7. The simulated vertical polarization and polarization differences at 37 and 85 GHz for dry snow as a function of IWP for a particle of 400 μm. The radiative properties of the wet snow hydrometeors under different melted fractions (f_m) were simulated for the particle number concentration calculated for dry snow and their size allowed to decrease to conserve the IWP. The simulated vertical polarization and polarization differences for dry snow with the SS PSD applied is also shown.

(i.e., a mixture of air and ice). The dielectric properties for dry snow were calculated using ice inclusions in an air matrix, but it is worth noting that using air inclusions in a matrix of ice yielded very similar results (not shown). The volume fraction of the ice inclusions was determined by applying the density parameterization from *Mitchell et al.* [1990] (see Table 1) to the snowflake diameter ($\rho_{ds}(D)$). Using the other parameterizations listed in Table 1 yielded very similar results, with differences in TBVH of the order of 1 K and in TBV of the order of 2 K at 85 GHz. Figure 5 evidences that the scattering is much more important at 85 GHz than that at 37 GHz for both pristine ice and dry snow hydrometeors, while comparing pristine ice with dry snow shows that dry snow has enhanced the scattering and the polarization differences. For large particles of dry snow that have a large scattering effect (TBVs lower than 160 K), TBVH reaches a limit where multiple scattering effects become significant and TBVH approaches a saturation limit and starts decreasing. For higher IWPs, the TBVH saturation limit is approached with smaller particle sizes. It is important to keep in mind, however, that a comparison between ice and dry snow equal size particles takes into account a decrease in density in the dry snow particles: this decrease in density translates into an increase in the particle number concentration. Clearly, for a given particle size, the increase of particle number increases the scattering effect, as well as the polarization difference. Due to this effect, Figure 5 evidences how important density can be as a parameter, specially at 85 GHz. Note that in Figure 5d, TBVH for dry snow particles (IWP=0.2 kg/m^2) of aspect ratios of 1, 1.2, and 1.4 are also shown for comparison.

[31] Figure 6 explores the effect of snow wetness by including different melted fractions (f_m) in the ice-air-water

mixture for an IWP of 0.4 kg/m^3. In the case of wet snow, since the integrated ice water path is maintained constant for a given particle size, an increase in melting fraction leads to an increase in density and to a decrease in particle number concentration. For realistically large particle sizes, when the melted fraction increases, the simulated TBV depressions and polarization differences are more limited. Tests were also run to evaluate the sensitivity of wet snow to the choice of $\rho_s(D)$ when calculating the dielectric properties of its dry snow matrix. This sensitivity was observed in the simulations to be not larger than 2 K for both TBVH and TBV at 85 GHz. In a cloud during the melting process, the transition from dry snow to melting snow does not induce a change of particle number concentration but a change in particle size, with the melting particle being smaller than the dry snow particle of the same mass. Figure 7 tests the effect of the melting fraction (f_m) for a given IWP, when conserving the particle number concentration. For each value of IWP and each hydrometeor phase, the particle number concentration is calculated for dry snow particles of 400 μm effective radius. For the wet hydrometeors simulated, in order to conserve IWP with the number concentration fixed to that of dry snow, their size is allowed to decrease. Figure 7 illustrates that for a given value of IWP and for a given particle number concentration, the change in dielectric properties from dry to wet snow does not compensate for the reduction in particle size that occurs in the melting layer.

[32] The simulations discussed so far with a monodisperse particle size distribution assess qualitatively the impact of hydrometeor dielectric properties on the polarization signal. In order to investigate more realistic clouds that contain particles of different size, the radiative transfer calculations for horizontally aligned ice particles were

repeated assuming an exponential particle size distribution for dry snow from *Sekhon and Srivastava* [1970]. The resulting magnitude of the depolarization (5–10 K) is comparable to the fixed particles size (Figure 7) and to the observed one (Figure 3). Then repeating the radiative transfer calculations with the *McFarquhar and Heymsfield* [1997] PSD parameterization for the same IWP range produces a maximum depolarization signal of approximately 3 K at 85 GHz (not shown).

[33] These simulations show that horizontally oriented oblate dry snow particles can generate the scattering signatures observed at 85 GHz, with polarization differences of the order of 5 K and higher. For a given IWP and particle size, dry snow is more efficient than pure ice at scattering and at generating polarized scattering at 85 GHz: the decrease in the real part of the refractive index from pure ice to dry snow, a mixture of ice and air, is largely compensated by the increase in particle number as a result of the lower density of dry snow. Melting of the snow does not enhance the brightness temperature depression nor the polarization difference. The changes in the real part of the refractive index from dry snow to melting snow do not compensate for the decrease in particle size that occurs with the melting of the particle.

5. Conclusion

[34] Scattering at 85 GHz over clouds is often associated with significant polarization differences (TBVH > 5 K), both over land and ocean. Coincident passive and active observations from TRMM show that a large portion of polarized scattering tends to occur when the radar observes a bright band, i.e., in the presence of a melting layer. The scattering signal by frozen particles is not only observable at 85 GHz when a melting layer is detected, but also at 37 GHz. Note nevertheless that, as expected, the magnitude of the TB decrease at 37 GHz is much more limited than at 85 GHz. Aggregation of snow particles around the 0°C isotherm produces large flakes that can significantly scatter the microwave. Our simulations show that the observations with TMI that coincide with a detected bright band on the PR can be interpreted in terms of dry snow particles of oblate bulk shapes with aspect ratios of the order of 1.6, and with horizontal orientation. The melting of the large snow flakes does not appear to increase the scattering effects.

[35] The sensitivity of passive microwave polarized scattering to the shape and orientation of the hydrometeors is unique among the current observations: it is an unexpected tool to gain understanding in complex microphysical processes in clouds.

[36] The presence of a melting layer can be deduced from the analysis of the polarized scattering signal, as shown in this study, with a rather stable relationship in the TBV and TBVH space when a radar bright band is observed. Neglecting the effect of the melting layer in the retrieval has been shown to lead to an overestimation of the precipitation for light stratiform rain [*Brown and Ruf*, 2007], a key issue in mid-latitude regions where the majority of the precipitation has a low freezing level. The Global Precipitation Measuring (GPM) mission will extend the TRMM capacity outside the Tropics to global and more frequent observations. Outside the regions where both passive and active observa-

tions from GPM will be available, the polarized scattering signal around 85 GHz can indicate the presence of the melting layer and will allow to redirect the retrieval scheme towards a more realistic precipitation scheme over land and ocean.

[37] The French-Indian Megha-Tropiques mission, launched in October 2011, carries a passive microwave conical scanner with polarized measurements at 18.7, 23.8, 36.5, 89, and 157 GHz. Analysis of the polarized scattering signal at 157 GHz is expected to begin soon: with a better sensitivity to the scattering by the ice phase, it will likely bring new insight into the cloud microphysics. These studies are also important in the framework of the development of the Ice Cloud Imager (ICI) for the next generation of European weather satellites, MetOp Second Generation (MetOp-SG). ICI is a radiometer planned to cover frequencies from 183 GHz up to 664 GHz.

Appendix A: Possible Links Between the Polarized Scattering Signatures at 85 GHz, and the Polarized Observations in the Visible

[38] The study was extended to a comparison of concurrent A-TRAIN observations of AMSR-E (Advanced Microwave Scanning Radiometer for EOS) and PARASOL instruments. The AMSR-E radiometer measures the microwave signal at 6.925, 10.65, 18.7, 23.8, 36.5, and 89.0 GHz. The PARASOL instrument, called POLDER (Polarization and Directionality of the Earth Reflectances) is a wide-field imaging radiometer/polarimeter [*Deschamps et al.*, 1994] that operates in the 443–1020 nm range with some polarized bands (443, 670, and 865 nm) [*Bréon and Dubrulle*, 2004]. PARASOL observations can be used to detect the sun glint, i.e., the reflection of the sun light in the visible and near infrared not only by the ice crystals located in the upper part of the clouds [*Noel and Chepfer*, 2004; *Bréon and Dubrulle*, 2004] but by lakes, oceans, or deserts. Some properties of the ice crystals that induce the sun glint such as their orientation can be deduced from PARASOL observations as well [*Noel and Chepfer*, 2004; *Bréon and Dubrulle*, 2004].

[39] The analysis was performed for all ascending orbits of 2006, i.e., daytime orbits over the 40°S–40°N latitude range. The method consists first in identifying and locating the sun glint in each PARASOL frame and, second, in deriving the properties of the ice crystals from the optical radiation measured at the sun glint locations. The radiometric signal at 89 GHz in V and H polarization comes from (almost) time-coincident AMSR-E observations measured at the nearest AMSR-E beam to the sun glint location pinpointed by PARASOL. The radiometric signal measured where sun glint occurs was investigated for ocean and land separately. It turns out that no specific radiometric signature at 89 GHz appears to be associated with sun glint. Indeed sun glint was detected in cloud regions characterized by a large range of brightness temperatures at 89 GHz (from 100 to 260 K). The absence of a specific radiometric signal associated with sun glint can be explained by the fact that even if horizontally oriented ice crystals are located at the top of the clouds, they can induce the sun glint measured by PARASOL, while the 89 GHz signal measured by AMSR-E is sensitive to a larger depth of hydrometeors below the

cloud top. However, submillimeter wave radiometers in conjunction with sun glint detection instruments should be used to study the properties of cloud ice and the interaction between hydrometeor orientation and polarization in the upper part of the clouds.

References

Armstrong, R. L., and M. J. Brodzik (2005), Northern hemisphere EASE-grid weekly snow cover and sea ice extent version 3 (Boulder, CO: National snow and ice data center, Digital Media), accessed May 2010 at http://nsidc.org/data/nsidc-0046.html.

Awaka, J., T. Iguchi, H. Kumagai, and K. I. Okamoto (1997), Rain type classification algorithm for TRMM precipitation radar, *Geoscience and Remote Sensing, 1997. IGARSS'97. Remote Sensing-A Scientific Vision for Sustainable Development*, vol. 4, pp. 1633–1635.

Battaglia, A., C. Kummerow, D.-B. Shin, and C. Williams (2003), Constraining microwave brightness temperatures by radar bright band observations, *J. Atmos. Oceanic Technol.*, *20*, 856–871.

Bauer, P., J. P. V. Poiares Baptista, and M. de Iulis (1999), The effect of the melting layer on the microwave emission of clouds over the ocean, *J. Atmos. Sci.*, *56*, 852–867.

Bauer, P., A. Khain, A. Pokrovsky, R. Meneghini, C. Kummerow, F. Marzano, and J. P. V. Poiares Baptista (2000), Combined cloud-microwave radiative transfer modeling of stratiform rainfall, *J. Atmos. Sci.*, *57*, 1082–1104.

Berg, W., T. L'Ecuyer, and J. M. Haynes (2010), The distribution of rainfall over oceans from spaceborne radars, *J. Appl. Meteorol. Clim.*, *49*, 535–543.

Botta, G., K. Aydin, and J. Verlinde (2010), Modeling of microwave scattering from cloud ice crystal aggregates and melting aggregates: A new approach, *IEEE Geosci. and Remote Sens. Lett.*, *7*, 572–576.

Bréon, F.-M., and B. Dubrulle (2004), Horizontally oriented plates in clouds, *J. Atmos. Sci.*, *61*, 2888–2898.

Brown, S. T., and C. S. Ruf (2007), Validation and development of melting layer models using constraints by active/passive microwave observations of rain and the wind-roughened ocean surface, *J. Atmos. Oceanic Technol.*, *24*, 543–563.

Chevallier, F., S. Di Michele, and A. P. Mc Nally, (2006), Diverse profile datasets from the ECMWF 91-level short-range forecasts, *Technical report, NWP SAF satellite application facility for numerical weather prediction*, Document no. NWPSAF-EC-TR-010, Version 1.0.

Cunningham, R. M. (1947), A different explanation of the bright line, *J. Meteor.*, *4*, 163.

Deschamps, P.-Y., F.-M. Breon, M. Leroy, A. Podaire, A. Bricaud, J.-C. Buriez, and G. Seze (1994), The POLDER mission: Instrument characteristics and scientific objectives, *IEEE Trans. Geosci. and Remote Sensing*, *32*, 598–615.

Di Girolamo, P., B. B. Demoz, and D. N. Whiteman (2003), Model simulations of melting hydrometeors: A new bright band from melting frozen drops, *Geophys. Res. Lett.*, *30*(12), 1626, doi:10.1029/2002GL016825.

Dungey, C. E., and C. F. Bohren (1993), Backscattering by non-spherical hydrometeors as calculated by the coupled-dipole method: An application in radar meteorology, *J. Atm. Oceanic Technol.*, *10*, 526–532.

Emde, C., S. A. Buehler, C. Davis, P. Eriksson, T. R. Sreerekha, and C. Teichmann (2004), A polarized discrete ordinate scattering model for simulations of limb and nadir longwave measurements in 1D/3D spherical atmospheres, *J. Geophys. Res.*, *109*, D24207, doi:10.1029/2004JD005140.

Eriksson, P., S. A. Buehler, C. P. Davis, C. Emde, and O. Lemke (2011), ARTS, the atmospheric radiative transfer simulator, Version 2, *J. Quant. Spectrosc. Radiat. Transfer*, *112*, 1551–1558.

Fabry, F., and W. Szyrmer (1999), Modeling of the melting layer. Part II: Electromagnetic, *J. Atmos. Sci.*, *56*, 3593–3600.

Hanesch, M. (1999), Fall velocity and shape of snowflakes, Dissertation ETH No 13322, Swiss Federal Institute of Technology, Zurich.

Iguchi, T., T. Kozu, R. Meneghini, J. Awaka, and K. Okamoto (2000), Rain-profiling algorithm for the TRMM precipitation radar, *J. Appl. Meteor.*, *39*, 2038–2052.

Kollias, P., and B. Albrecht (2005), Why the melting layer radar reflectivity is not bright at 94 GHz, *Geophys. Res. Lett.*, *32*, L24818, doi:10.1029/2005GL024074.

Korolev, A., and G. Isaac (2003), Roundness and aspect ratio of particles in ice clouds, *J. Atmos. Sci.*, *60*, 1795–1808.

Kummerow, C., W. Barnes, T. Kozu, J. Shiue, and J. Simpson (1998), The tropical rainfall measuring mission (TRMM) sensor package, *J. Atmos. Oceanic Technol.*, *15*, 809–817.

Kummerow, C., et al. (2000), The status of the tropical rainfall measuring mission (TRMM) after two years in orbit, *J. Appl. Meteor.*, *39*, 1965–1982.

Kulie, M. S., R. Bennartz, T. J. Greenwald, Y. Chen, and F. Weng (2010), Uncertainties in microwave properties of frozen precipitation: Implications for remote sensing and data assimilation, *J. Atmos. Sci.*, *67*, 3471–3487.

Matrosov, S. Y., A. J. Heymsfield, and Z. Wang (2005), Dual-frequency radar ratio of nonspherical atmospheric hydrometeors, *Geophys. Res. Lett.*, *32*, L13816, doi:10.1029/2005GL023210.

McFarquhar, G. M., and A. J. Heymsfield (1997), Parameterization of tropical cirrus ice crystal size distributions and implications for radiative transfer: Results from CEPEX, *J. Atmos. Sci.*, *54*, 2187–2200.

Meirold-Mautner, I., C. Prigent, E. Defer, J. R. Pardo, J.-P. Chaboureau, J.-P. Pinty, M. Mech, and S. Crewell (2006), Radiative transfer simulations using mesoscale cloud model outputs: Comparisons with passive microwave and infrared satellite observations for midlatitudes, *J. Atmos. Sci.*, *64*, 1550–1568.

Meneghini, R., and L. Liao (1996), Comparisons of cross sections for melting hydrometeors as derived from dielectric mixing formulas and a numerical method, *J. Appl. Meteor.*, *35*, 1658–1670.

Meneghini, R., and L. Liao (2000), Effective dielectric constants of mixed-phase hydrometeors, *J. Atmos. Oceanic Technol.*, *17*, 628–640.

Mishchenko, M. I. (2000), Calculation of the amplitude matrix for a non-spherical particle in a fixed orientation, *Appl. Opt.*, *39*, 1026–1031.

Mitchell, D. L., R. Zhang, and R. L. Pitter (1990), Mass-dimensional relationships for ice particles and the influence of riming on snowfall rates, *J. Appl. Meteor.*, *29*, 153–163.

Mitra, S. K., O. Vohl, M. Ahr, and H. R. Pruppacher (1990), A wind tunnel and theoretical study of the melting behavior of atmospheric ice particles. IV: Experiment and theory of snowflakes, *J. Atmos. Sci.*, *47*, 584–591.

Mohr, K. I., J. S. Famiglietti, and E. J. Zipser (1999), The contribution to tropical rainfall with respect to convective system type, size, and intensity estimated from the 85-GHz ice-scattering signature, *J. Appl. Meteor.*, *38*, 596–606.

Noel, V., and H. Chepfer (2004), Study of ice crystal orientation in cirrus clouds based on satellite polarized radiance measurements, *J. Atmos. Sci.*, *61*, 2073–2081.

Liao, L., and R. Meneghini (2005), On modeling air/spaceborne radar returns in the melting layer, *IEEE Trans. Geo. Remote Sens.*, *43*, 2799–2809.

Liao, L., and R. Meneghini (2009), Validation of TRMM precipitation radar through comparison of its multiyear measurements with ground-based radar, *J. Appl. Meteor. Climatol.*, *48*, 804–817.

Locatelli, J. D., and P. V. Hobbs (1974), Fall speeds and masses of solid precipitation particles, *J. Geophys. Res.*, *79*(15), 2185–2197, doi:10.1029/JC079i015p02185.

Olson, W. S., P. Bauer, N. F. Viltard, D. E. Johnson, W.-K. Tao, R. Meneghini, and L. Liao (2001a), A melting-layer model for passive/active microwave remote sensing applications. Part I: Model formulation and comparison with observations, *J. Appl. Meteor.*, *40*, 1145–1163.

Olson, W. S., P. Bauer, C. D. Kummerow, Y. Hong, and W. K. Tao (2001b), A melting-layer model for passive/active microwave remote sensing applications. Part II: Simulation of TRMM observations, *J. Appl. Meteorol.*, *40*, 1164–1179.

Prigent, C., J. R. Pardo, M. I. Mishchenko, and W. B. Rossow (2001), Microwave polarized scattering signatures in clouds: SSM/I observations interpreted with radiative transfer simulations, *J. Geophys. Res*, *106*, 28,243–28,258.

Prigent, C., E. Defer, J. R. Pardo, C. Pearl, W. B. Rossow, and J.-P. Pinty (2005), Relations of polarized scattering signatures observed by TRMM microwave instrument with electrical processes in cloud systems, *Geophys. Res. Lett.*, *32*, L04810, doi:10.1029/2004GL022225.

Sassen, K., S. Matrosov, and J. Campbell (2007), CloudSat spaceborne 94 GHz radar bright bands in the melting layer: An attenuation-driven upside-down lidar analog, *Geophys. Res. Lett.*, *34*, L16818, doi:10.1029/2007GL030291.

Schols, J. L., J. A. Weinman, G. D. Alexander, R. E. Stewart, L. J. Angus, and A. C. L. Lee (1999), Microwave properties of frozen precipitation around a North Atlantic Cyclone, *J. Appl. Meteor.*, *38*, 29–43.

Sekhon, R. S., and R. C. Srivastava (1970), Snow size spectra and radar reflectivity, *J. Atmos. Sci.*, *27*, 299–307.

Schumacher, C., and R. A. Houze Jr. (2000), Comparison of radar data from the TRMM satellite and Kwajalein Oceanic validation site, *J. Appl. Meteorol.*, *39*, 2151–2164.

Surussavadee, C., and D. H. Staelin (2006), Comparison of AMSU millimeter-wave satellite observations, MM5/TBSCAT predicted radiances, and electromagnetic models for hydrometeors, *IEEE Trans. Geo. Remote Sens.*, *44*, 2667–2678.

Willis, P. T., and A. J. Heymsfield (1989), Structure of the melting layer in mesoscale convective system stratiform precipitation, *J. Atmos. Sci.*, *46*, 2008–2025.

Xie, X., U. Lhnert, S. Kneifel, and S. Crewell (2012), Snow particle orientation observed by ground-based microwave radiometry, *J. Geophys. Res.*, *117*, D02206, doi:10.1029/2011JD016369.

Xie, X., and J. Miao (2011), Polarization difference due to nonrandomly oriented ice particles at millimeter/submillimeter waveband, *J. Quant. Spectrosc. Ra.*, *112*, 1090–1098.

Zawadzki, I., W. Szyrmer, C. Bell, and F. Fabry (2005), Modeling of the melting layer. Part III: The density effect, *J. Atmos. Sci.*, *62*, 3705–3723.